

# Surface Ir<sup>+5</sup> Formation as a Universal Prerequisite for O<sub>2</sub> Evolution on Ir Oxides

Nataša Diklić, Adam H. Clark, Juan Herranz,\* Dino Aegerter, Justus S. Diercks, Alexandra Beard, Viktoriia A. Saveleva, Piyush Chauhan, Maarten Nachtegaal, Thomas Huthwelker, Dmitry Lebedev, Paula Kayser, José Antonio Alonso, Christophe Copéret, and Thomas J. Schmidt



Cite This: *ACS Catal.* 2023, 13, 11069–11079



Read Online

ACCESS |



Metrics & More



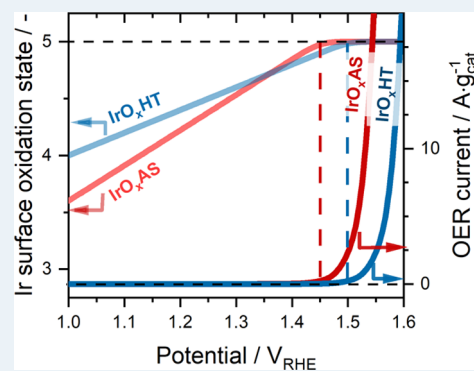
Article Recommendations



Supporting Information

**ABSTRACT:** The large-scale deployment of polymer electrolyte water electrolysis (PEWE) is largely limited by the use of O<sub>2</sub> evolution reaction (OER) catalysts based on scarce and expensive iridium in PEWE anodes. The ensuing need for better-performing, Ir-based OER catalysts requires an improved understanding of the relation between these materials' activity and their physicochemical *operando* properties. To shed light on this matter, here, we employed *operando* modulation excitation X-ray absorption spectroscopy to determine the oxidation state of surface Ir in a range of Ir oxides with different surface compositions, crystal structures, and OER activities. Our results reveal that, irrespectively of these diverging properties, the surface Ir in all catalysts systematically undergoes a linear, potential-driven oxidation that stabilizes once a +5 state is reached. The completion of this surface oxidation process is then showed to correlate with the onset of O<sub>2</sub> evolution, thus strongly hinting at the involvement of Ir in oxidation states  $\geq +5$  in the OER and indirectly discarding those mechanisms that do not consider such states as a part of the reaction sequence.

**KEYWORDS:** OER, IrO<sub>2</sub> catalysts, electrochemistry, *operando* XAS, modulation excitation XAS



## INTRODUCTION

Hydrogen plays a pivotal role in all roadmaps toward a net zero society, and polymer electrolyte water electrolyzers (PEWEs) are excellently suited for their green production under the dynamic conditions entailed by the electrification of these devices with intermittent, renewable energy.<sup>1</sup> However, the sluggish kinetics of the oxygen evolution reaction (OER) occurring in PEWE anodes lead to large efficiency losses that drastically increase these electrolyzers' operational costs. Furthermore, the high price and scarcity<sup>2</sup> of the Ir oxides used to catalyze the OER ( $\approx 5000$  \$ oz<sub>Ir</sub><sup>-1</sup> and  $< 9$  t<sub>Ir-mined</sub> y<sup>-1</sup>, respectively)<sup>2,3</sup> limit future PEWE installation capacity. This calls for novel materials with enhanced OER activities whose design shall be guided by an improved understanding of the interfacial processes that dictate the performance of state-of-the-art Ir-based catalysts under reaction conditions.

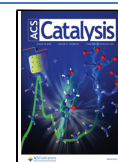
The extensive research allocated to this crucial topic has led to establish a qualitative relation between the crystalline structure of Ir oxides and their OER performance, whereby amorphous oxides generally show a superior activity compared to their crystalline counterparts.<sup>4–7</sup> Based on the results of *ex situ* characterization, this correlation has been shown to result from the higher content of cationic and anionic surface defects (Ir<sup>+3</sup> vs. electrophilic oxygen species, respectively) in such disordered materials.<sup>7–11</sup> Additionally, a wide range of Ir oxides have been investigated by means of *operando/in situ*

techniques, including Raman,<sup>12–14</sup> ultraviolet–visible (UV–VIS),<sup>15–17</sup> X-ray absorption,<sup>5,18–23</sup> or X-ray photoelectron<sup>24–27</sup> spectroscopies (XAS or XPS, respectively). The results of these studies have reinforced the relation between the oxides' OER activity and their (sub)surface content of *operando*-generated, electrophilic oxygen species, which are believed to participate in the O–O coupling step of the OER mechanism.<sup>25,27,28</sup> However, the latter reaction sequence remains unresolved, and no consensus has been reached on such an elementary matter like the oxidation state of the Ir surface under operative conditions. Specifically, *operando* XPS studies have pointed at a surface Ir oxidation state of +4<sup>25,26,29</sup> or +5,<sup>30</sup> whereas *in situ/operando* XAS works have suggested values of +3.8,<sup>18</sup> +4.5,<sup>23</sup> +4.8,<sup>19</sup> or +5,<sup>5,20,21,31</sup> whereby the latter agrees with the conclusions of *in situ/operando* UV–VIS spectroscopy measurements.<sup>15,16</sup> These inconsistencies in the assignment of the Ir oxidation state likely stem from differences in the types of Ir oxides, probing techniques (i.e., bulk- vs.

**Received:** March 30, 2023

**Revised:** June 26, 2023

**Published:** August 7, 2023



surface-sensitive), cell designs,<sup>30,32</sup> and/or experimental conditions<sup>30,32</sup> used in those studies, which additionally lacked reference compounds for the reliable assignment of the Ir in oxidation states  $>+4$  to back up their conclusions.

In an effort to fill these knowledge gaps, in this study, we have carried out a detailed physico- and electrochemical characterization of four Ir oxides with different crystallinities, surface compositions, and OER activities and used these materials to investigate the relation between their *operando* surface Ir oxidation state and catalytic performance. To this end, we have performed *operando* modulation excitation X-ray absorption spectroscopy (ME-XAS) measurements with an enhanced sensitivity to the interfacial species<sup>33</sup> involved in the OER. Our results reveal that, despite the large differences among catalysts, all of them undergo an oxidation of their interfacial sites to an Ir<sup>+5</sup> state and that the completion of this oxidation process systematically coincides with the OER onset. As such, these findings strongly hint at the direct involvement of this highly oxidized intermediate in the reaction mechanism.

## EXPERIMENTAL SECTION

**Catalysts.** Four different Ir oxide electrocatalysts were used in this study. Two catalysts were commercially available iridium oxide powders from Alfa Aesar (Premion, 99.99%, metals basis) and Umicore CO & AG (batch number: BRO 0469 A1), and they were denoted in this text as IrO<sub>x</sub> AA and IrO<sub>x</sub> Umi, respectively. Out of the other two catalysts, IrO<sub>x</sub> AS was synthesized using the Adams fusion method, and part of this sample was heat treated, resulting in the IrO<sub>x</sub> HT sample. Details on IrO<sub>x</sub> synthesis along with the preparation of reference materials for Ir in a higher oxidation state (i.e., +5 and +6) can be found in the [Methods](#) section of the Supporting Information.

**Electrochemical Measurements in a Rotating Disk Electrode (RDE) Setup.** OER performance of IrO<sub>x</sub> catalysts was evaluated in a standard three-electrode glass cell (Pine Research Instrumentation) filled with 0.1 M perchloric acid (prepared from HClO<sub>4</sub>, Veritas double distilled, GFS chemicals) using a rotating disk electrode (RDE). A glassy carbon disk (5 mm diameter, SIGRADUR G, HTW Hochtemperatur-Werkstoffe GmbH) embedded in a poly-etheretherketone (PEEK) RDE (Pine Research Instrumentation) served as the working electrode on which the catalyst was deposited. Catalyst ink was prepared by mixing 10 mg of catalyst, 4 mL of isopropyl alcohol (99.9%, HPLC Plus, Sigma-Aldrich), 1 mL of ultrapure water, and 20  $\mu$ L of Nafion solution ( $\approx$ 5 wt % Nafion perfluorinated resin solution, Sigma-Aldrich) and sonicating 30 min in an ultrasonication bath. Following a thin-film RDE approach,<sup>34</sup> the catalyst ink was then deposited on the electrode by a spin-coating method used in ref 35 to yield the final catalyst loading of 100  $\mu$ g cm<sup>-2</sup>. For all RDE measurements, gold mesh and Hg/HgSO<sub>4</sub> electrodes were used as counter and reference electrodes.

Prior to measuring polarization curves, cyclic voltammograms (CVs) were recorded between 1.00 and 1.40 V<sub>RHE</sub> at 50 and 10 mV s<sup>-1</sup>. The Ohmic drop was corrected by performing electrochemical impedance spectroscopy measurements at 1 V<sub>RHE</sub> between 1 MHz and 1 Hz and with an amplitude of 10 mV. Finally, polarization curves were obtained by holding potential for 1 min between 1.20 and 1.56 V<sub>RHE</sub>. Current plotted represents the last point of such holds.

**X-ray Absorption Spectroscopy.** *Ex situ* XAS measurements at the O K edge were performed at the PHOENIX

beamline of the Swiss Light Source (SLS-Villigen, Switzerland). All spectra were recorded in total electron yield (TEY) mode in high vacuum ( $\approx$ 10<sup>-5</sup> mbar). The photon energy was tuned in the range between 510 and 600 eV, and the TEY signal was collected measuring the current flowing from the ground toward the sample holder. The catalyst powder samples were prepared on conductive carbon tape ensuring that the layer of the catalyst was thick enough to neglect any contributions of this carbon tape to the measured signal.

Complementarily, XAS spectra at the Ir L<sub>3</sub> edge were collected at the SuperXAS beamline of the SLS.<sup>36</sup> A polychromatic beam provided by a 2.9 T bending magnet was collimated by a Rh-coated mirror at 2.9 mrad and monochromatized using a channel-cut Si(111) monochromator cooled with liquid nitrogen. The beam was focused by a Rh-coated double focusing mirror. To avoid radiation damage, recently shown to be critical to obtain reliable results,<sup>35</sup> the beam intensity was reduced by 80% for all measurements by placing a 320  $\mu$ m thick Al foil before the first ionization chamber, as to lead to an intensity of  $\approx$ 2.5  $\times$  10<sup>12</sup> photons mm<sup>-2</sup> s<sup>-1</sup>. The final size of the beam on the sample was 0.4  $\times$  1 mm<sup>2</sup>. *Operando* XAS measurements were carried out at the Ir L<sub>3</sub> edge using quick scanning mode (i.e., quick scanning extended X-ray absorption fine structure, QEXAFS) with a monochromator oscillation frequency of 1 Hz. The Ir L<sub>3</sub> spectra were collected in fluorescence mode using a 500  $\mu$ m thick passivated implanted planar silicon (PIPS) detector (Mirion Technologies).<sup>37</sup> To calibrate the beamline energy, a piece of Pt foil was placed between the second and third gas ionization chambers filled with N<sub>2</sub> (at 2.5 bar) and the energy of the Pt L<sub>3</sub>-edge was set to 11,564 eV. For *ex situ* measurements, the samples and standard materials were pelletized with cellulose (Sigma-Aldrich) as a diluent and were measured in transmission mode. More details on electrode preparation for *operando* measurements and data analysis can be found in the [Methods](#) section of the Supporting Information.

**Electrochemical Protocol of Operando XAS Measurement.** Before starting the measurement, both the working and the counter electrodes were pretreated by pipetting a droplet of ultrapure water on top of the catalyst layers (CLs) placed in a desiccator that was then closed and pressure-reduced to  $\approx$ 50 mbar in order to evacuate gas trapped within the catalyst layer pores.<sup>38</sup> Prior to each *operando* measurement, the utilization of the working electrode CL was assessed by recording cyclic voltammograms at 50 and 10 mV s<sup>-1</sup> between 1.00 and 1.40 V<sub>RHE</sub>, after which the electrodes were conditioned by performing a chronopotentiometric hold at 30 mA cm<sup>-2</sup> until the potential of the working electrode stopped decreasing (typically requiring  $\approx$ 5 min; see [Figure S1](#)). This conditioning step was performed in order to remove air still embedded within the CL pores. After conditioning, the CL utilization was assessed again as to make sure that a full utilization was achieved.

Following this initial electrochemical characterization of each electrode, the *operando* ME-XAS part of the experiment was conducted as following:

Sinusoidal stimulus ME-XAS was employed using sinusoidal voltammetry with a frequency of 0.01 Hz between a lower inversion potential and an upper inversion potential ( $E_{\text{lower}}$  vs.  $E_{\text{upper}}$ , respectively).  $E_{\text{lower}}$  was kept to be 1.00 V<sub>RHE</sub> throughout the whole experiment, while  $E_{\text{upper}}$  was chosen to correspond to a potential below the OER onset or within the OER region.

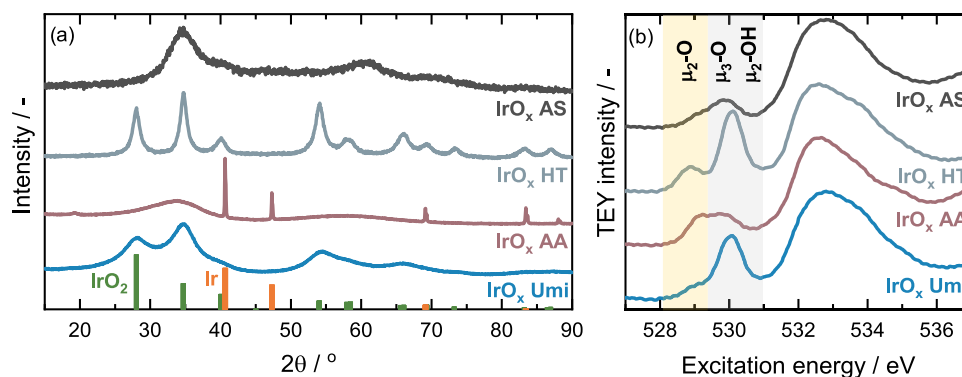


**Figure 1.** X-ray diffraction patterns (a) and O K edge total electron yield X-ray absorption spectra (b) acquired on the IrO<sub>x</sub> AS, IrO<sub>x</sub> HT, IrO<sub>x</sub> AA, and IrO<sub>x</sub> Umi powders. The reference diffraction patterns of rutile IrO<sub>2</sub> and metallic Ir (ICSD database<sup>45</sup> collection codes 81028 vs. 64992, respectively) are indicated as green and orange bars in panel “a”.

In this first part of the experiment, this higher potential was never higher than 1.60 V<sub>RHE</sub>, as to avoid large currents and the concomitant impact of oxygen bubbles accumulated in the catalyst layer (and possibly leading to catalyst delamination)<sup>35</sup> on the spectral quality and reliability of the results. Table S1 lists the potentials chosen for each specific material in each part of the experiment. As IrO<sub>x</sub> AS was the most active catalyst, the potentials applied were 50 mV lower compared to the other catalysts. For each  $E_{\text{upper}}$  value, 25 sinusoidal potential cycles were acquired.

Subsequently, the pulsed ME-XAS part of the experiment consisted of potential steps between  $E_{\text{lower}}$  and  $E_{\text{upper}}$  (with the specific potential values listed in Table S1), with 25 s holds at each potential and 10 repetitions of each potential sequence. In this part of the experiment, the higher inversion potentials were also kept below 1.60 V<sub>RHE</sub> to avoid bubble accumulation and catalyst delamination as much as possible. Notably, the results derived from these measurements are in qualitative agreement with those inferred from the sinusoidal ME tests described above and below, and since they do not add any additional insight to the conclusions reached in this study, they are not discussed here.

Finally, step (i) was repeated using  $E_{\text{upper}}$  values > 1.6 V<sub>RHE</sub> (again listed in Table S1) for IrO<sub>x</sub> AS, HT, and Umi.

**XAS Data Treatment.** The energy alignment of O K edge spectra was performed by shifting the spectra from IrO<sub>2</sub> Sigma-Aldrich (99.9% metal basis) for a certain extent so that  $\mu_3$ -O peak maxima correspond to an energy of 530.1 eV<sup>25,27</sup> and subsequently shifting the spectra of other materials for the same quantity. For the data processing, the pre-edge was fitted with a line which was then subtracted from the acquired spectra to result the ones shown herein. For the comparison and verification of this method, spectra were also normalized using Athena software from the Demeter package.<sup>39</sup> As the main message herein is drawn from extracted intensity ratios of O K edge pre-peaks, those ratios were compared between the spectra that were normalized and the ones that are obtained by subtracting the pre-edge line. Those pre-peak ratios (i.e.,  $\mu_2$ -O/( $\mu_3$ -O +  $\mu_2$ -OH)) are shown to be similar using both methods for data treatment, and thus, we have chosen the latter method for its simplicity and avoiding additional uncertainties that can be imposed by spectra normalization (i.e., choosing different post-edge normalization ranges lead to significant changes in O K edge spectra among materials, caused by short post-edge range of data acquired herein).

ProQEXAFS<sup>40</sup> software was used to calibrate the energy of collected spectra, as well as to perform spectra averaging and normalization. For modulation excitation experiments, sinusoidal and pulse voltage stimuli were used with a period of 100 and 50 s, respectively. To improve the signal-to-noise ratio in those data, 2 spectra were averaged in the case of sinusoidal ME experiment, while no spectra averaging was used for pulse experiments leading to a period of 50 s in both cases. Subsequently, 25 cycles in sinusoidal and 10 cycles in pulse mode were period-averaged, and phase-resolved spectra were then obtained by demodulating period-averaged data using python scripts according to the following equation<sup>33,41</sup>

$$I_n(E, \phi_k^{\text{PSD}}) = \frac{2}{T} \int_0^T I(E, t) \cdot \sin(k\omega t + \phi_k^{\text{PSD}}) dt$$

where  $T$  is the period,  $\omega$  is the modulation frequency,  $k$  is the demodulation index,  $\phi_k^{\text{PSD}}$  is the phase angle for demodulation  $k$ ,  $I(E, t)$  is the response of the system in the time domain, and  $I_n(E, \phi_k^{\text{PSD}})$  in the frequency domain.

## RESULTS AND DISCUSSION

**Materials' Ex Situ Characterization.** To rationalize the OER performance and spectroscopic response of the four catalysts included in this study under *operando* conditions (see discussion below), we start our work by discussing the results derived from their characterization with various complementary, *ex situ* techniques. Transmission electron microscopy and selected-area electron diffraction (TEM and SAED, respectively; see Figure S2) reveal that the IrO<sub>x</sub> AS sample prepared *in house* through the Adams fusion method (see the Methods section of the Supporting Information for details) possesses the smallest particle size ( $\approx 1.5$  nm), in good agreement with previous studies of Ir oxides synthesized using this approach.<sup>7,11,42,43</sup> Heat treating a fraction of this material as to yield the second lab-synthesized IrO<sub>x</sub> HT sample led to an increase in particle size ( $\geq 5$  nm) and crystallinity, as indicated by the fringes visible in the TEM images and the additional presence of discrete diffraction spots (on top of the customary rings) in the SAED pattern.<sup>44</sup> On the other hand, the first commercial oxide purchased from Alfa Aesar (IrO<sub>x</sub> AA) consists of interconnected particles with poorly defined edges and attenuated fringes indicative of an amorphous matrix. Finally, the second commercial catalyst provided by Umicore (IrO<sub>x</sub> Umi) consists of agglomerated nanocrystals leading to an electron diffractogram featuring rings assignable to rutile-



**Table 1.** Surface and Bulk Average Iridium Oxidation States Derived from *Ex Situ* Ir 4f XP- vs. Ir L<sub>3</sub> XA-Spectra, along with the Ratio between Peak Intensities of the  $\mu_2$ -O and the Sum of  $\mu_3$ -O and  $\mu_2$ -OH Species (at  $\approx 529$  vs.  $\approx 530$  eV, Respectively, in Figure 1b) Inferred from the O K Edge Total Electron Yield XAS<sup>a</sup>

material	bulk oxidation state <sup>b</sup> (XAS)	surface oxidation state <sup>c</sup> (XPS)	$\mu_2\text{-O}/(\mu_3\text{-O} + \mu_2\text{-OH})$	$j$ at 1.525 $V_{\text{RHE}}/\text{A g}_{\text{cat}}^{-1}$	capacitive charge/C $\text{g}_{\text{cat}}^{-1}$	TOF at 1.525 $V_{\text{RHE}}/\text{s}^{-1}$
IrO <sub>x</sub> AS	+4.1	+3.6	0.60	70 $\pm$ 9	114 $\pm$ 8	0.60 $\pm$ 0.09
IrO <sub>x</sub> HT	+4.2	+4	0.31	11.2 $\pm$ 0.4	45 $\pm$ 1	0.24 $\pm$ 0.01
IrO <sub>x</sub> AA	+3.9	+3.8	1.00	38 $\pm$ 3	176 $\pm$ 3	0.22 $\pm$ 0.02
IrO <sub>x</sub> Umi	+4	+4	0.24	4.2 $\pm$ 0.9	23 $\pm$ 2	0.19 $\pm$ 0.02

<sup>a</sup>Also listed are the mass-normalized OER currents and corresponding turn over frequencies (TOFs) at 1.525  $V_{\text{RHE}}$ , whereby the latter are estimated based on the mass-normalized capacitive charges recorded in cyclic voltammograms between 1.00 and 1.40  $V_{\text{RHE}}$  (see Figure S10) that also appear in the table. Note that all reported errors correspond to standard deviations based on a minimum of three independent repetitions. <sup>b</sup>A detailed explanation of the procedures followed to infer the Ir oxidation state based on the XAS WL position is provided in Supporting Information Note 1. <sup>c</sup>The average oxidation states derived from Ir 4f XP-spectra were inferred by weighing each Ir oxidation state (i.e., +4 or +3) with their percentual areas in the deconvoluted spectra (displayed in Tables S4–S7).

like IrO<sub>2</sub> (i.e., the  $P4_2/mnm$  structure of IrO<sub>2</sub>, referred to “rutile IrO<sub>2</sub>” in what follows) whose broadness can be linked to the oxide’s small crystallite size. Complementarily, the surface areas (SAs) derived for all catalysts on the basis of N<sub>2</sub>-sorption measurements are summarized in Table S2, whereby the small particle size of the IrO<sub>x</sub> AS catalyst leads to this sample featuring the highest SA ( $\approx 330 \text{ m}^2 \text{ g}^{-1}$ ).

Additionally, we assessed the crystallinity of these materials using X-ray diffraction (XRD; see Figure 1a), which unveiled that (in agreement with previous studies and based on the comparison with the diffraction patterns of IrO<sub>2</sub> and metallic Ir)<sup>8,45</sup> the IrO<sub>x</sub> AA catalyst possesses an amorphous structure with contributions of metallic Ir that are expected to account for  $\approx 2$ –3 wt % of the catalyst’s total Ir mass.<sup>8</sup> On the other hand, the diffractogram recorded on the IrO<sub>x</sub> Umi sample features broad rutile peaks stemming from the small crystallite size discussed above, whereas the pattern of the IrO<sub>x</sub> HT catalyst also exhibits rutile-related peaks with an enhanced sharpness caused by its larger crystallite size. As for the IrO<sub>x</sub> AS sample, its XRD pattern is similar to the one reported for an Ir oxide previously prepared through the same synthesis approach<sup>7,11</sup> and displays broad peaks that cannot be assigned to known crystalline phases of any Ir-based compounds.<sup>11</sup>

The four catalyst powders were further characterized by *ex situ* XAS in order to determine the average oxidation state of all of their Ir atoms (i.e., taking advantage of XAS’ intrinsic bulk sensitivity). To this end, we carried out complementary XAS measurements on a number of reference Ir compounds with oxidation states ranging between +3 and +6 (see the Methods section in the Supporting Information for more details). We then established a linear relation between their oxidation state and the position of the white line (WL) maximum in their X-ray absorption near-edge structure (XANES) spectra (see Supporting Information Note 1 along with Figures S3 and S4). As summarized in Table 1, the catalysts’ average Ir oxidation states derived from these XAS measurements span between +3.9 and +4.2 (for IrO<sub>x</sub> AS vs. IrO<sub>x</sub> HT, respectively) and are further endorsed by the results of complementary temperature-programmed reduction (TPR) measurements listed in Table S3 (see also Supporting Information Note 2 and Figures S5 and S6).

On top of these results derived from bulk-sensitive techniques, we also assessed the catalysts’ surface properties by performing XPS measurements and carefully deconvoluting their Ir 4f spectra (see Figure S7 and Tables S4–S7). While currently there is no consensus among the XPS community on the best practice to tackle this Ir 4f spectral deconvolu-

tion,<sup>8,28,30,46</sup> we did so by following the procedure proposed by Pfeifer et al.<sup>8</sup> that has been largely adopted in recent years.<sup>11,25,47,48</sup> Pending on the uncertainties associated to this fitting approach, the derived results point at the presence of Ir<sup>+3</sup> species on the (sub)surface of the IrO<sub>x</sub> AS and IrO<sub>x</sub> AA samples (whereby Ir<sup>+3</sup> components account for  $\approx 37$  vs.  $\approx 22\%$  of the total spectral areas, respectively), whereas the spectra acquired of IrO<sub>x</sub> Umi and IrO<sub>x</sub> HT could be satisfactorily fitted using only Ir<sup>+4</sup> species (see values listed in Table 1). Complementarily, the distribution of O-species within the catalysts’ (sub)surfaces was investigated by means of O K edge XAS measurements in total electron yield (TEY) mode. The acquired spectra are shown in Figure 1b and systematically feature two pre-edge peaks (with their intensity ratios differing among catalysts—see Table 1) at  $\approx 529$  and  $\approx 530$  eV (see Figure S8a for an enlarged representation of this area). The lower energy peak reportedly arises from electrophilic, surface oxygen species (also referred to as  $\mu_2$ -O),<sup>8,25,27,28</sup> whereas the higher energy one can be assigned to bulk oxygen (or  $\mu_3$ -O—see refs 8, 25, 27, 28 and the spectrum of a rutile IrO<sub>2</sub> reference compound in Figure S8b) and/or to hydroxide-terminated surface sites (so-called  $\mu_2$ -OH species).<sup>25,28</sup> Notably, those  $\mu_2$ -OH surface groups are expected to feature a  $\approx 60\%$  lower resonance intensity than the bulk  $\mu_3$ -O sites.<sup>28</sup> Thus, the pre-edge feature at  $\approx 530$  eV in the spectrum of the high-surface-area amorphous IrO<sub>x</sub> AS catalyst can be mostly assigned to  $\mu_2$ -OH groups, whereas for the low-surface-area rutile-like IrO<sub>x</sub> HT and IrO<sub>x</sub> Umi samples, this same peak preponderantly relates to abundant  $\mu_3$ -O sites. Finally, both peaks feature similar intensities in the spectrum of the IrO<sub>x</sub> AA catalyst, indicating that this material (along with IrO<sub>x</sub> HT) possesses the highest concentrations of surface  $\mu_2$ -O sites.

**Electrochemical Performance.** Following this *ex situ* characterization of all four IrO<sub>x</sub> catalysts, their OER activity was evaluated in RDE configuration employing protocols explained in detail in the Methods section of the Supporting Information. The derived Tafel plots are displayed in Figure S9, and their Tafel slopes and catalytic activities (expressed as mass-normalized currents at 1.525  $V_{\text{RHE}}$ ) are summarized in Tables S8 and 1, respectively. The sample with the highest surface area, IrO<sub>x</sub> AS, unambiguously exhibits the highest OER activity ( $\approx 70 \text{ A g}_{\text{cat}}^{-1}$  at 1.525  $V_{\text{RHE}}$ ), in line with the values reported for similarly prepared materials).<sup>11,42</sup> This is followed by IrO<sub>x</sub> AA (with  $\approx 38 \text{ A g}_{\text{cat}}^{-1}$ ), which features a  $\approx 10$ -fold lower surface area (see Table S2) but, as discussed above, is also an amorphous oxide with a high content of activity-enhancing electronic defects in cationic and anionic frameworks (i.e., Ir<sup>+3</sup>

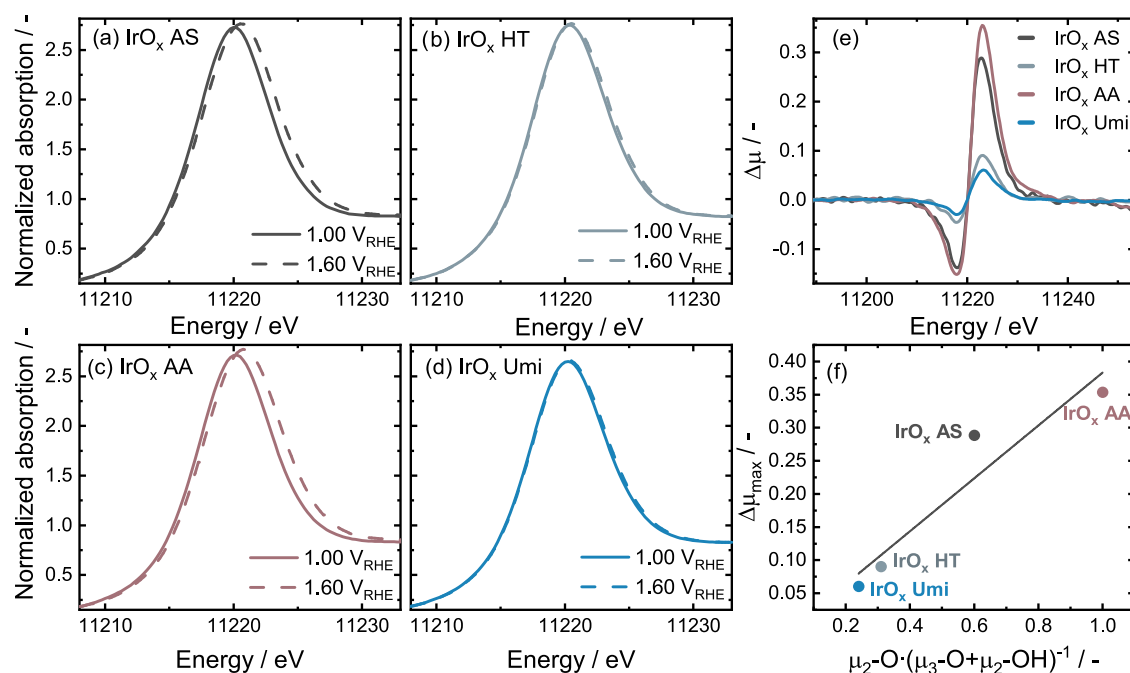


**Figure 2.** XANES spectra acquired at 1.00 and 1.60  $V_{\text{RHE}}$  on  $\text{IrO}_x$  AS (a),  $\text{IrO}_x$  HT (b),  $\text{IrO}_x$  AA (c), and  $\text{IrO}_x$  Umi (d). Difference of the spectra acquired at 1.60 and 1.00  $V_{\text{RHE}}$  for all materials ( $\Delta\mu$ ) (e) and relation between the magnitude of the maximum of the spectral difference ( $\Delta\mu_{\text{max}}$ ) and the ratio of oxygen species extracted from the O K edge XAS measurements (f).

and electrophilic surface oxygen species, respectively).<sup>7,8,10,49</sup> Moreover, the calcination of  $\text{IrO}_x$  AS to yield  $\text{IrO}_x$  HT decreases its surface area and OER performance  $\approx 8$  vs. 7-fold, respectively (to  $\approx 44 \text{ m}^2 \text{ g}^{-1}$  and  $\approx 11 \text{ A g}_{\text{cat}}^{-1}$ ). However, despite its higher crystallinity (see the XRD and SAED results above), this heat-treated sample still outperforms the  $\text{IrO}_x$  Umi catalyst (featuring  $\approx 4 \text{ A g}_{\text{cat}}^{-1}$ ), possibly (and at least in part) because the latter features a  $\approx 4$ -fold lower surface area than  $\text{IrO}_x$  HT (again, see Table S2).

To take into account the possible effect of the different surface areas of these materials on their OER activity, the corresponding currents were normalized by the capacitive charges shown in Figure S9b, as to yield the TOF values listed in Table 1. Note that those capacitive charges should be proportional to the catalyst electrochemical surface areas, and were derived from the CVs featured in Figure S10. This normalization confirmed that the  $\text{IrO}_x$  AS sample possesses the greatest intrinsic activity, in line with the high content of surface  $\text{Ir}^{3+}$  inferred from the XPS results as well as the large concentration of  $\mu_2\text{-O}$  sites observed in the TEY-XAS results.<sup>25,27,28</sup> On the other hand, after this charge normalization, the intrinsic activity of the  $\text{IrO}_x$  AA catalyst remains  $\approx 3$ -fold lower than that of  $\text{IrO}_x$  AS, possibly because the latter features a lower surface Ir oxidation state (Table 1). Complementarily,  $\text{IrO}_x$  AA displays a higher relative content of subsurface  $\mu_2\text{-O}$  that has been correlated with the OER activity of Ir oxides.<sup>8,9</sup> In this regard, Massué et al.<sup>10</sup> suggested that the availability of  $\mu_2\text{-O}$  species, which is probably dependent on the catalyst structure, determines whether reactants can reach those active sites. As such, although  $\text{IrO}_x$  AA contains the highest relative content of electrophilic  $\mu_2\text{-O}$  species, this catalyst's low surface area likely implies that a large fraction of those  $\mu_2\text{-O}$  sites are located in its subsurface. Thus, while those functionalities can participate in (pseudo)-capacitive processes (justifying this material's large capacitance—see Figure S11a, which includes the data for a large

number of Ir oxides featured in previous works),<sup>7,11</sup> the OER is likely to lead to the fast accumulation of evolved  $\text{O}_2$ -bubbles within the catalyst's subsurface. These would in turn shield those sites and preclude their subsequent involvement in the reaction, leading to the relatively low specific OER activity (i.e., TOF) featured by this material despite its amorphous nature. In contrast to this, the  $\text{IrO}_x$  AS sample possesses a significantly smaller particle size (and correspondingly higher surface area) that implies a higher availability of truly surface-accessible  $\mu_2\text{-O}$  groups and translates in the higher intrinsic OER activity exhibited by this material.

Beyond this observation, the intrinsic OER performances exhibited by the more oxidized  $\text{IrO}_x$  Umi and  $\text{IrO}_x$  HT samples are remarkably close to those of the amorphous  $\text{IrO}_x$  AA catalyst. As it can be seen in Figure S11b,c, though, no clear correlation can be established between the TOFs of these and other Ir oxides and their  $\text{N}_2$ -sorption surface areas or double layer capacitive charges, indicating that none of those variables exclusively determines these oxides' surface-specific OER activity.

**Operando XAS Results.** Following this assessment of the four catalysts' physico- and electrochemical properties, we proceeded to study their behavior under OER conditions by performing *operando* XAS measurements using a spectroelectrochemical flow cell described in detail in refs 50, 51. The complete electrochemical utilization of the samples' CLs was first confirmed based on the good overlap of the mass-normalized CVs recorded in the *operando* flow cell and in RDE configuration (using loadings of  $\approx 300$ – $900$  vs.  $\approx 100 \mu\text{g}_{\text{catalyst}} \text{ cm}^{-2}$ , respectively; see Figure S10 and the Methods section of the Supporting Information for details on the procedures of electrode preparation).<sup>11,52</sup> The electrodes were then electrochemically conditioned by holding the current at  $30 \text{ mA cm}^{-2}$  until the potential stopped decreasing (typically  $\approx 5$  min). This conditioning entails a significant performance improvement (e.g., for  $\text{IrO}_x$  AS, a  $\approx 3$ -fold increase in the OER current at

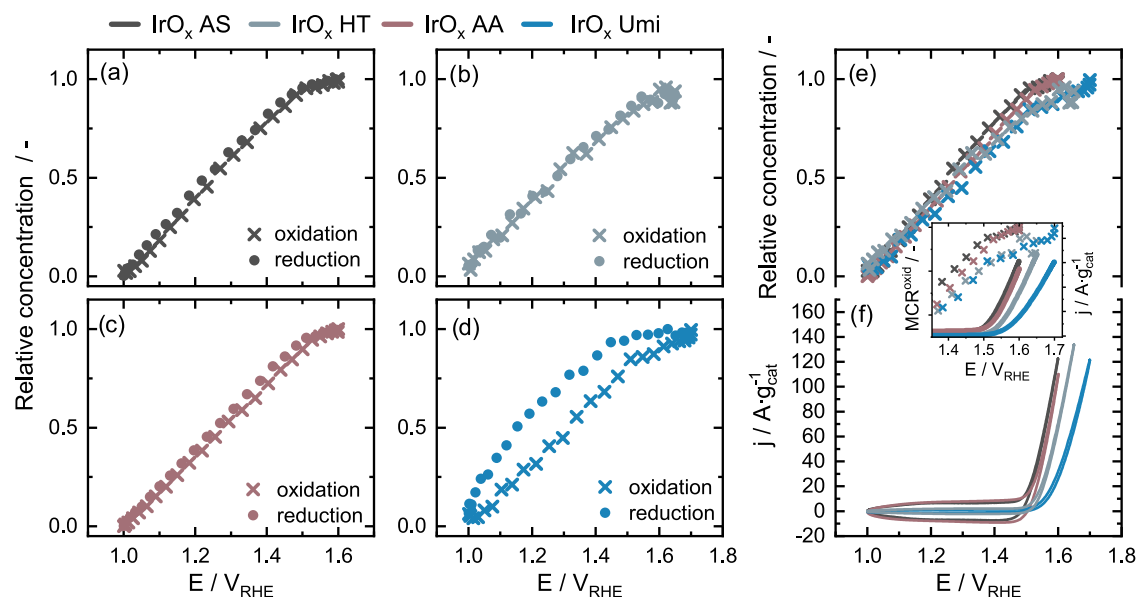


**Figure 3.** Relative concentration of the MCR<sup>ox</sup> component obtained from the MCR analysis of the period-averaged XAS data for IrO<sub>x</sub> AS (a), IrO<sub>x</sub> HT (b), IrO<sub>x</sub> AA (c), and IrO<sub>x</sub> Umi (d), with corresponding  $E_{upper}$  values of 1.60, 1.65, 1.60, and 1.70  $V_{RHE}$ , respectively, and both in the positive- and negative-going potential scan directions (i.e., oxidation vs. reduction). Comparison of all four catalysts' relative MCR<sup>ox</sup> concentrations (e) and their sinusoidal voltammetry electrochemical response (f) with the inset displaying a magnification of the potential region around the catalysts' OER onsets coinciding with the plateauing of the corresponding MCR<sup>ox</sup> concentrations.

1.60  $V_{RHE}$ ; see Figure S1) that renders the *operando* XAS results discussed below fully representative of the catalysts' behavior under OER conditions. We note in passing that we have also verified the stability of all tested electrodes and the absence of experimental artifacts related to beam damage,<sup>35</sup> as discussed in Supporting Information Note 3 and shown in Figures S12 and S13.

Following this important conditioning step and verifications, Figure 2a–d shows the *operando* XANES spectra acquired on all four IrO<sub>x</sub> catalysts at 1.00 and 1.60  $V_{RHE}$ . Interestingly, all spectra at the higher potential exhibit a shift of the WL toward higher energies and feature an increased WL area that can be assigned to Ir oxidation.<sup>18–20,23,53–55</sup> Moreover, the magnitude of this shift (and corresponding extent of oxidation) varies significantly among the catalysts and can be quantified as the difference between the spectra acquired at the two potentials (or so-called “ $\Delta\mu$  spectra”),<sup>56–59</sup> which appears displayed in Figure 2e. Therein, the shape of these difference spectra is similar for all materials (see also the charge-normalized  $\Delta\mu$  spectra in Figure S14a), indicating that the Ir in the four catalysts undergoes similar changes. Complementarily, the large divergence in  $\Delta\mu$  spectral magnitudes among catalysts suggests a bigger extent of oxidation for IrO<sub>x</sub> AS and IrO<sub>x</sub> AA compared to the IrO<sub>x</sub> HT and IrO<sub>x</sub> Umi catalysts. This might appear counterintuitive for the IrO<sub>x</sub> AA catalyst since based on XAS' bulk sensitivity, one would expect a small potential-induced spectral change for such a low surface area material.<sup>7</sup> In this regard, Figure S14b shows that for all other three catalysts, a linear correlation is found between the maximum of their difference spectra ( $\Delta\mu_{max}$ ) and their N<sub>2</sub>-sorption SAs, whereas IrO<sub>x</sub> AA appears as an outlier in that graph. However, when this relation is reassessed using the electrochemical capacitive charge as a metric representative of the catalysts' surface area, a linear trend between this parameter and  $\Delta\mu_{max}$  is found for all four materials, as shown in Figure S14c. Thus, the larger spectral change observed for IrO<sub>x</sub> AS and IrO<sub>x</sub> AA vs.

IrO<sub>x</sub> HT and IrO<sub>x</sub> Umi exclusively stems from the higher content of electrochemically active sites in these two, more amorphous materials. Moreover, Figure S15 reveals a linear relation between this capacitive charge and the catalysts  $\mu_2$ -O (sub)surface content. It is worth noting that even if our  $\mu_2$ -O contents are derived from *ex situ* measurements, a similar relation between capacitive charge and the concentration of *operando*-generated  $\mu_2$ -O groups has recently been pointed out by Nong et al.,<sup>55</sup> thus hinting at a correlation between the contents of *ex situ* and *operando*-generated  $\mu_2$ -O groups. Most importantly, our results show that this *ex situ* variable is also correlated with the oxidation extent (i.e.,  $\Delta\mu_{max}$ ), as illustrated in Figure 2f, emphasizing the idea that these groups are involved in the charge storage process.

To shed light on these activity-determining parameters, we proceeded to perform *operando* XAS measurements with a sinusoidal stimulus in quick acquisition mode by sinusoidally cycling the potential 25 times between 1.00  $V_{RHE}$  and various upper inversion potentials ( $E_{upper}$ ), whereby the  $E_{upper}$  value was individually adjusted for each catalyst as to yield resembling OER currents for all tested materials (see Supporting Information Note 4 and the values summarized in Table S1). The derived, time-resolved XAS data was first period-averaged and then analyzed by means of multivariate curve resolution (MCR), which systematically yielded two spectral components with absorption edges at lower vs. higher incident X-ray energies and which are therefore referred to as reduced vs. oxidized species (i.e., MCR<sup>re</sup> or MCR<sup>ox</sup>, respectively) in what follows. Examples of these MCR components for the modulation events with the highest  $E_{upper}$  values tested for each catalyst are displayed in Figure S16, whereby the observed changes in spectral magnitude and shape qualitatively resemble the ones observed as a function of the applied potential in Figure 2.

Furthermore, the MCR analysis also yields concentration profiles of the inferred components (see Figure S17) which we

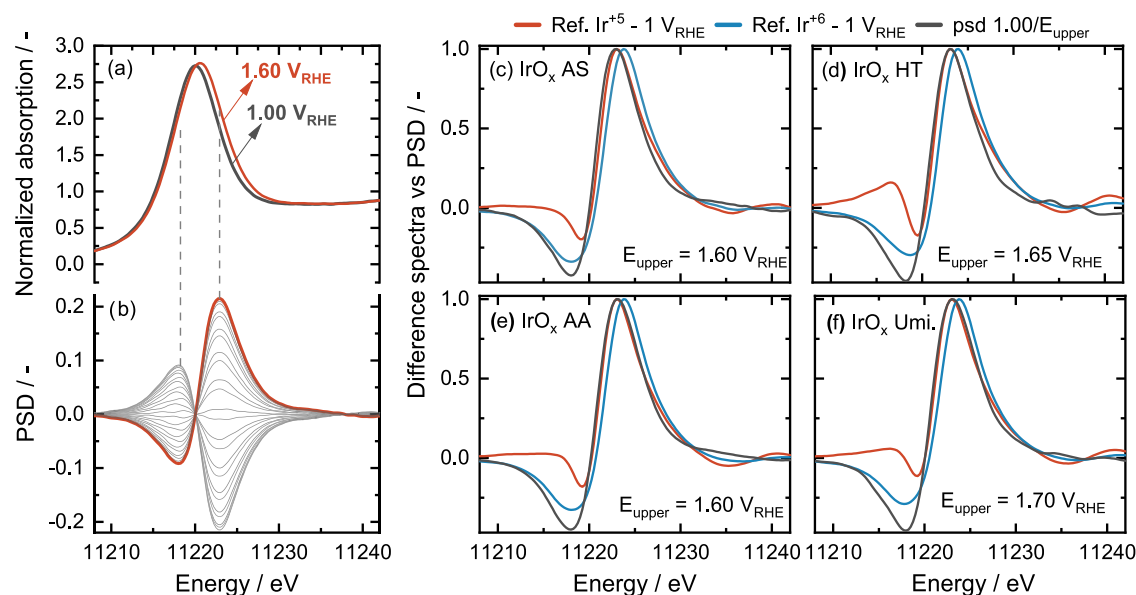


**Figure 4.** Operando XAS spectra acquired on the IrO<sub>x</sub> AS catalyst at 1.00 and 1.60 V<sub>RHE</sub> (a) and corresponding phase-resolved spectra ( $\phi^{\text{PSD}} = 0-360^\circ$ , in  $15^\circ$  increments) based on a sinusoidal stimulus with  $E_{\text{upper}} = 1.60$  V<sub>RHE</sub> (b). Comparison between the PSD spectra of IrO<sub>x</sub> AS (c), IrO<sub>x</sub> HT (d), IrO<sub>x</sub> AA (e), and IrO<sub>x</sub> Umi (f) (in each case, based on potential modulations with the  $E_{\text{upper}}$  values indicated in the respective panels) and the difference between the spectra of Ir<sup>+5</sup> or Ir<sup>+6</sup> reference compounds (Sr<sub>2</sub>YIrO<sub>6</sub> vs. Sr<sub>2</sub>CaIrO<sub>6</sub>, respectively) and the spectrum recorded at 1.00 V<sub>RHE</sub> on each catalyst. Note that in panels “c” to “f”, the PSD spectral intensities have been normalized by their maximum values in order to facilitate the comparison among the spectra of the different catalysts.

transferred from the time to the potential scales, thanks to the synchronized recording of both variables within the *operando* XAS data acquisition system. Thus, the relative concentrations of the MCR<sup>ox</sup> component as a function of potential for each of the tested catalysts are featured in Figure 3a–d (and the corresponding MCR<sup>re</sup> concentration profiles appear in Figure S18). A first observation derived from this analysis is that all catalysts except IrO<sub>x</sub> Umi feature an excellent overlap between the content of the MCR<sup>ox</sup> component (and the MCR<sup>re</sup> one too; see Figure S18) in the positive- and negative-going potential directions. The IrO<sub>x</sub> Umi catalyst, however, displays a hysteresis that indicates that these redox processes take place at different rates depending on the potential scan direction. Notably, the opposite behavior (i.e., slower oxidation than reduction) has been reported in time-resolved, *operando* XAS studies of Pt-nanoparticle<sup>60,61</sup> and Fe-based single-atom<sup>62</sup> catalysts for which these slower oxidation rates were tentatively related to O-adsorption strengths and corresponding differences in O<sub>2</sub> reduction activities. Analogously, the sluggish reduction at high potentials observed for the IrO<sub>x</sub> Umi catalyst could be indicative of slow O-desorption and of an excessive O-binding energy that could explain this sample’s meager OER performance. However, considering that on a TOF basis the latter OER activity is not significantly different from that of the IrO<sub>x</sub> HT and IrO<sub>x</sub> AA catalysts (see Figure S9) for which such a hysteresis is not observed, along with the mechanistic discussion reported in what follows, this hypothesis remains highly tentative.

Beyond these uncertainties, it becomes evident that the relative content of each MCR<sup>ox</sup> component is both potential- and catalyst-dependent since during the positive-going (i.e., oxidative) potential sweeps, their concentration increases linearly until plateauing at a given potential whose specific value is sample-dependent (see Figure S19). To help visualize this sample-dependent relations between applied potential and Ir oxidation plateau and contextualize this result with regards

to the samples’ OER activities, Figure 3e,f compares the potential-dependent MCR<sup>ox</sup> concentration profiles with the corresponding currents recorded on each catalyst during these sinusoidal voltammetries. Interestingly, this comparison unveils that for all materials, the beginning of the Ir oxidation plateau generally overlaps with the corresponding OER onset, implying that the start of this Faradic reaction first requires for the whole catalyst to reach a specific (and complete) oxidation state. This behavior is in stark contrast with many other electrocatalytic processes in which the reaction can already proceed on surfaces/sites partially transformed to the catalytically active oxidation state (see e.g., the reduction of O<sub>2</sub> on Mn oxides, Pt or single-atom catalysts)<sup>63–65</sup> and implies that the subsequent OER mechanism is decoupled from the oxidation of the IrO<sub>x</sub> surface. Notably, this plateauing of the oxidation state is in agreement with previous *operando* studies<sup>12,15–17,31,66</sup> that, on the other hand, only dealt with amorphous Ir oxides or a single-atom Ir catalyst and is also qualitatively similar to the relation between applied potential and capacitive charge found by Nong et al.<sup>55</sup> for several Ir-based OER catalysts (i.e., amorphous or calcined Ir(Ni) oxides) based on purely electrochemical measurements. Thus, our results show for the first time that this maxing of the Ir oxidation state with the OER onset is universally applicable to Ir oxides with different crystalline structures and surface compositions.

Following this important finding, we focus on unveiling the actual oxidation state(s) that trigger the OER process. Chiefly, the Ir oxidation state assignment remains a matter of vivid debate since the studies mentioned above were not able to precisely determine the *operando* oxidation number (and could only qualitatively ascribe it to values  $>+4$ )<sup>12,17</sup> or attributed it to an oxidation state of +5 based on UV–VIS spectra of Ir<sup>+5</sup> complex compounds or without actual reference spectra (in ref 16 vs. refs 21, 31, respectively). Therefore, we applied phase-sensitive detection (PSD) on the period-averaged XAS spectra dataset acquired during the sinusoidal potential stimulus and



obtained the phase-resolved spectra displayed in Figures S20–S23 for all materials. Interestingly, as shown in Figure S24a, the shape and energy positions of the demodulated spectra maxima and minima for a given  $E_{\text{upper}}$  value are similar for all catalysts, thus indicating that all materials undergo similar, potential-induced structural and/or electronic modifications. On top of this and analogous to what was observed for the  $\Delta\mu$  spectra, their PSD amplitude for a given  $E_{\text{upper}}$  value scales linearly with the mass-normalized capacitive charges, indicating that these PSD spectra are also sensitive to the extent of the changes inferred to the materials by the sinusoidal stimulus (see Figure S24b).

To better illustrate the origin of these spectral differences, Figure 4a,b features exemplary XANES spectra recorded on the  $\text{IrO}_x$  AS catalyst at 1.00 and 1.60  $V_{\text{RHE}}$  and the corresponding PSD spectra recorded with the same  $E_{\text{upper}}$  value. The larger intensity features in the PSD spectrum appear within the XANES region, with only small changes being discernible in the extended X-ray absorption fine structure region (see Figures S20–S23). Moreover, the PSD maximum is located at energies slightly above the XANES maximum and can therefore be regarded as representative of a change in the spectral broadness that, as discussed above, would render this feature sensitive to changes in the oxidation state.

On this basis, we interpret the phase-resolved spectra acquired with  $E_{\text{upper}}$  values chosen to assure that all materials were already in the oxidation state plateau (see Figure 3e) by comparing them with the difference between the spectrum of each sample at the lower inversion potential of 1.00  $V_{\text{RHE}}$  and those of reference compounds with well-defined Ir oxidation states.<sup>67</sup> Specifically, for the higher oxidation numbers of +5 and +6, we employed  $\text{Sr}_2\text{YIrO}_6$  and  $\text{Sr}_2\text{CaIrO}_6$  double perovskites<sup>68–71</sup> as the reference compounds, respectively. The results of these comparisons are displayed in Figure 4c–f, whereby the overlap of the PSD and the difference spectra obtained with the  $\text{Ir}^{+5}$  reference compound along their maxima unambiguously implies that the Ir in all materials systematically oxidizes to a +5 state at OER potentials, irrespective of the catalysts' initial crystallinity and surface properties.

Notably, Ooka et al.<sup>16</sup> recently suggested that the accumulation of Ir +5 is a prerequisite for the OER but only showed this for an electrodeposited amorphous Ir oxide. Thus, our findings generalize the importance of this effect, which applies to all Ir oxides irrespectively of their crystalline structure and/or surface composition. Moreover, our results discard the validity of OER mechanisms that proceed exclusively through O-mediated redox cycles<sup>25,26</sup> since these only entail the involvement of Ir in oxidation states  $\leq +4$  in the reaction. We note in passing that even for the remaining mechanisms invoking the active involvement of  $\text{Ir}^{+5}$  in the OER process, the formation of short-lived intermediate species with Ir oxidation states above or below +5 cannot be excluded<sup>6</sup> since such intermediates would only be shortly present on the catalyst surface and/or would entail irreversible changes (e.g., Ir dissolution and/or lattice oxygen evolution) that cannot be tackled in such modulation excitation measurements.

On the other hand, in analogy with other studies including multiple Ir oxides synthesized via different routes,<sup>10,55</sup> we could not identify a physicochemical (*operando*) property that can universally describe these materials' surface-specific OER activity. We believe that this will require further developments in *operando* techniques that can discriminate truly interfacial vs.

subsurface processes while using operatively relevant electrochemical setups (e.g., fed with liquid water as a reactant).

## CONCLUSIONS

In summary, our *operando* ME-XAS measurements on four  $\text{IrO}_x$  OER catalysts with different crystallinities and surface chemistries show that all  $\text{IrO}_x$  catalysts undergo an oxidation of their surfaces prior to the start of the OER process. Thanks to this technique's enhanced surface sensitivity and the novel use of reference Ir compounds with oxidation states  $\geq +5$ , we prove for the first time that this common oxidation state corresponds to Ir +5. The completion of this surface oxidation process is then showed to correlate with the onset of  $\text{O}_2$  evolution on all catalysts, strongly hinting at the involvement of this Ir +5 state in the OER while indirectly discarding those mechanisms that do not invoke the oxidation of Ir up to this state as a part of the reaction process.

## ASSOCIATED CONTENT

### Supporting Information

The Supporting Information is available free of charge at <https://pubs.acs.org/doi/10.1021/acscatal.3c01448>.

Detailed procedures followed for the synthesis of  $\text{IrO}_x$ -AS and  $\text{IrO}_x$ -HT; physicochemical characterization of all materials; preparation of electrodes; deconvolution of X-ray photoelectron spectra; transmission electron microscopy and selected-area electron diffraction of the four catalysts; *ex situ* XPS; hard and soft X-ray XAS and TPR results; electrochemical behavior in RDE tests; and additional results derived from the detailed processing of the *in situ* modulation excitation XAS data (PDF)

## AUTHOR INFORMATION

### Corresponding Author

Juan Herranz – Paul Scherrer Institut, 5232 Villigen PSI, Switzerland; [orcid.org/0000-0002-5805-6192](https://orcid.org/0000-0002-5805-6192); Email: [juan.herranz@psi.ch](mailto:juan.herranz@psi.ch)

### Authors

Nataša Diklić – Paul Scherrer Institut, 5232 Villigen PSI, Switzerland  
Adam H. Clark – Paul Scherrer Institut, 5232 Villigen PSI, Switzerland; [orcid.org/0000-0002-5478-9639](https://orcid.org/0000-0002-5478-9639)  
Dino Aegerter – Paul Scherrer Institut, 5232 Villigen PSI, Switzerland; [orcid.org/0000-0002-0965-5818](https://orcid.org/0000-0002-0965-5818)  
Justus S. Diercks – Paul Scherrer Institut, 5232 Villigen PSI, Switzerland  
Alexandra Beard – Paul Scherrer Institut, 5232 Villigen PSI, Switzerland  
Viktoriia A. Saveleva – Paul Scherrer Institut, 5232 Villigen PSI, Switzerland  
Piyush Chauhan – Paul Scherrer Institut, 5232 Villigen PSI, Switzerland; [orcid.org/0000-0002-2155-6193](https://orcid.org/0000-0002-2155-6193)  
Maarten Nachttegaal – Paul Scherrer Institut, 5232 Villigen PSI, Switzerland; [orcid.org/0000-0003-1895-9626](https://orcid.org/0000-0003-1895-9626)  
Thomas Huthwelker – Paul Scherrer Institut, 5232 Villigen PSI, Switzerland  
Dmitry Lebedev – Department of Chemistry and Applied Biosciences, ETH Zürich, CH-8093 Zürich, Switzerland; Present Address: Department of Materials Science and Engineering, Northwestern University, Evanston, Illinois 60208, United States; [orcid.org/0000-0002-1866-9234](https://orcid.org/0000-0002-1866-9234)



Paula Kayser – Instituto de Ciencia de Materiales de Madrid, C.S.I.C., E-28049 Madrid, Spain

José Antonio Alonso – Instituto de Ciencia de Materiales de Madrid, C.S.I.C., E-28049 Madrid, Spain; [orcid.org/0000-0001-5329-1225](https://orcid.org/0000-0001-5329-1225)

Christophe Copéret – Department of Chemistry and Applied Biosciences, ETH Zürich, CH-8093 Zürich, Switzerland; [orcid.org/0000-0001-9660-3890](https://orcid.org/0000-0001-9660-3890)

Thomas J. Schmidt – Paul Scherrer Institut, 5232 Villigen PSI, Switzerland; Laboratory of Physical Chemistry, ETH Zürich, CH-8093 Zürich, Switzerland; [orcid.org/0000-0002-1636-367X](https://orcid.org/0000-0002-1636-367X)

Complete contact information is available at:  
<https://pubs.acs.org/10.1021/acscatal.3c01448>

## Author Contributions

All authors have given approval to the final version of the manuscript.

## Funding

The financial support from the Swiss Federal Office of Energy (SFOE) and Umicore GmbH & Co KG is greatly acknowledged. J.A.A. and P.K. thank the financial support of the Spanish Ministry of Science and Innovation through the project MAT2017-84496-R.

## Notes

The authors declare no competing financial interest.

## ACKNOWLEDGMENTS

N.D. is thankful to Viktor Wolf for providing the IrO<sub>x</sub> Umi catalyst and, together with Daniel Herein, for scientific discussions. The authors also thank ScopeM for the use of their electron microscopy facilities. N.D. is thankful to Elisabeth Agnes Müller Gubler for all discussions and help with electron diffraction, to Casey Beall, Julia Linke, and Natasha Rose Hales for the help during sXAS measurements, and to Artsiusheuski Mikalai for the help with TPR experiments.

## ABBREVIATIONS

PEWE:polymer electrolyte water electrolysis; OER:oxygen evolution reaction; UV–VIS:ultraviolet–visible spectroscopy; XAS:X-ray absorption spectroscopy; XPS:X-ray photoelectron spectroscopy; RDE:rotating disk electrode; PEEK:polyether-etherketone; CV:cyclic voltammetry; ME-XAS:modulation excitation X-ray absorption spectroscopy; TEM:transmission electron microscopy; SAED:selected-area electron diffraction; SA:surface area; XRD:X-ray diffraction; WL:white line; XANES:X-ray absorption near-edge structure; QEXAFS:quick scanning extended X-ray absorption fine structure; TPR:temperature-programmed reduction; TEY:total electron yield; TOF:turn over frequency; CL:catalyst layer; MCR:multivariate curve resolution; PSD:phase-sensitive detection

## REFERENCES

- (1) Ayers, K.; Danilovic, N.; Harrison, K.; Xu, H. PEM Electrolysis, a Forerunner for Clean Hydrogen. *Electrochem. Soc. Interface* **2021**, *30*, 67–71.
- (2) Vesborg, P. C. K.; Jaramillo, T. F. Addressing the terawatt challenge: scalability in the supply of chemical elements for renewable energy. *RSC Adv.* **2012**, *2*, 7933–7947.

- (3) Matthey, J. PGM Management. <https://matthey.com/products-and-markets/pgms-and-circularity/pgm-management> (accessed June 1, 2022).

- (4) Geiger, S.; Kasian, O.; Shrestha, B. R.; Mingers, A. M.; Mayrhofer, K. J. J.; Cherevko, S. Activity and Stability of Electrochemically and Thermally Treated Iridium for the Oxygen Evolution Reaction. *J. Electrochem. Soc.* **2016**, *163*, F3132–F3138.

- (5) Minguzzi, A.; Locatelli, C.; Lugaresi, O.; Achilli, E.; Cappelletti, G.; Scavini, M.; Coduri, M.; Masala, P.; Sacchi, B.; Vertova, A.; Ghigna, P.; Rondinini, S. Easy Accommodation of Different Oxidation States in Iridium Oxide Nanoparticles with Different Hydration Degree as Water Oxidation Electrocatalysts. *ACS Catal.* **2015**, *5*, 5104–5115.

- (6) Kasian, O.; Grote, J. P.; Geiger, S.; Cherevko, S.; Mayrhofer, K. J. J. The Common Intermediates of Oxygen Evolution and Dissolution Reactions during Water Electrolysis on Iridium. *Angew. Chem., Int. Ed.* **2018**, *57*, 2488–2491.

- (7) Abbott, D. F.; Lebedev, D.; Waltar, K.; Povia, M.; Nachttegaal, M.; Fabbri, E.; Copéret, C.; Schmidt, T. J. Iridium Oxide for the Oxygen Evolution Reaction: Correlation between Particle Size, Morphology, and the Surface Hydroxo Layer from Operando XAS. *Chem. Mater.* **2016**, *28*, 6591–6604.

- (8) Pfeifer, V.; Jones, T. E.; Velasco Vélez, J. J.; Massué, C.; Arrigo, R.; Teschner, D.; Girgsdies, F.; Scherzer, M.; Greiner, M. T.; Allan, J.; Hashagen, M.; Weinberg, G.; Piccinin, S.; Hävecker, M.; Knop-Gericke, A.; Schlögl, R. The electronic structure of iridium and its oxides. *Surf. Interface Anal.* **2016**, *48*, 261–273.

- (9) Pfeifer, V.; Jones, T. E.; Velasco Velez, J. J.; Massue, C.; Greiner, M. T.; Arrigo, R.; Teschner, D.; Girgsdies, F.; Scherzer, M.; Allan, J.; Hashagen, M.; Weinberg, G.; Piccinin, S.; Havecker, M.; Knop-Gericke, A.; Schlogl, R. The electronic structure of iridium oxide electrodes active in water splitting. *Phys. Chem. Chem. Phys.* **2016**, *18*, 2292–2296.

- (10) Massué, C.; Pfeifer, V.; van Gastel, M.; Noack, J.; Algara-Siller, G.; Cap, S.; Schlogl, R. Reactive Electrophilic O(I-) Species Evidenced in High-Performance Iridium Oxohydroxide Water Oxidation Electrocatalysts. *ChemSusChem* **2017**, *10*, 4786–4798.

- (11) Povia, M.; Abbott, D. F.; Herranz, J.; Heinritz, A.; Lebedev, D.; Kim, B.-J.; Fabbri, E.; Patru, A.; Kohlbrecher, J.; Schäublin, R.; Nachttegaal, M.; Copéret, C.; Schmidt, T. J. Operando X-ray characterization of high surface area iridium oxides to decouple their activity losses for the oxygen evolution reaction. *Energy Environ. Sci.* **2019**, *12*, 3038–3052.

- (12) Pavlovic, Z.; Ranjan, C.; Gao, Q.; van Gastel, M.; Schlögl, R. Probing the Structure of a Water-Oxidizing Anodic Iridium Oxide Catalyst using Raman Spectroscopy. *ACS Catal.* **2016**, *6*, 8098–8105.

- (13) Pavlovic, Z.; Ranjan, C.; van Gastel, M.; Schlogl, R. The active site for the water oxidising anodic iridium oxide probed through in situ Raman spectroscopy. *Chem. Commun.* **2017**, *53*, 12414–12417.

- (14) Zou, S.; Chan, H. Y. H.; Williams, C. T.; Weaver, M. J. Formation and Stability of Oxide Films on Platinum-Group Metals in Electrochemical and Related Environments As Probed by Surface-Enhanced Raman Spectroscopy: Dependence on the Chemical Oxidant. *Langmuir* **2000**, *16*, 754–763.

- (15) Ooka, H.; Takashima, T.; Yamaguchi, A.; Hayashi, T.; Nakamura, R. Element strategy of oxygen evolution electrocatalysis based on in situ spectroelectrochemistry. *Chem. Commun.* **2017**, *53*, 7149–7161.

- (16) Ooka, H.; Wang, Y.; Yamaguchi, A.; Hatakeyama, M.; Nakamura, S.; Hashimoto, K.; Nakamura, R. Legitimate intermediates of oxygen evolution on iridium oxide revealed by in situ electrochemical evanescent wave spectroscopy. *Phys. Chem. Chem. Phys.* **2016**, *18*, 15199–15204.

- (17) Bozal-Ginesta, C.; Rao, R. R.; Mesa, C. A.; Liu, X.; Hillman, S. A. J.; Stephens, I. E. L.; Durrant, J. R. Redox-State Kinetics in Water-Oxidation IrO<sub>x</sub> Electrocatalysts Measured by Operando Spectroelectrochemistry. *ACS Catal.* **2021**, *11*, 15013–15025.

- (18) Pauporté, T.; Aberdam, D.; Hazemann, J.-L.; Faure, R.; Durand, R. X-ray absorption in relation to valency of iridium in sputtered iridium oxide films. *J. Electroanal. Chem.* **1999**, *465*, 88–95.
- (19) Hüppauff, M.; Lengeler, B. Valency and Structure of Iridium in Anodic Iridium Oxide Films. *J. Electrochem. Soc.* **1993**, *140*, 598–602.
- (20) Nong, H. N.; Reier, T.; Oh, H.-S.; Gliech, M.; Paciok, P.; Vu, T. H. T.; Teschner, D.; Heggen, M.; Petkov, V.; Schlögl, R.; Jones, T.; Strasser, P. A unique oxygen ligand environment facilitates water oxidation in hole-doped IrNiOx core–shell electrocatalysts. *Nat. Catal.* **2018**, *1*, 841–851.
- (21) Minguzzi, A.; Lugaresi, O.; Locatelli, C.; Rondinini, S.; D'Acapito, F.; Achilli, E.; Ghigna, P. Fixed energy X-ray absorption voltammetry. *Anal. Chem.* **2013**, *85*, 7009–7013.
- (22) Czioska, S.; Boubnov, A.; Escalera-López, D.; Geppert, J.; Zagalskaya, A.; Röse, P.; Saraçi, E.; Alexandrov, V.; Krewer, U.; Cherevko, S.; Grunwaldt, J.-D. Increased Ir–Ir Interaction in Iridium Oxide during the Oxygen Evolution Reaction at High Potentials Probed by Operando Spectroscopy. *ACS Catal.* **2021**, *11*, 10043–10057.
- (23) Hillman, A. R.; Skopek, M. A.; Gurman, S. J. X-ray spectroscopy of electrochemically deposited iridium oxide films: detection of multiple sites through structural disorder. *Phys. Chem. Chem. Phys.* **2011**, *13*, 5252–5263.
- (24) Sanchez Casalongue, H. G.; Ng, M. L.; Kaya, S.; Friebel, D.; Ogasawara, H.; Nilsson, A. In situ observation of surface species on iridium oxide nanoparticles during the oxygen evolution reaction. *Angew. Chem., Int. Ed.* **2014**, *53*, 7169–7172.
- (25) Saveleva, V. A.; Wang, L.; Teschner, D.; Jones, T.; Gago, A. S.; Friedrich, K. A.; Zafeirotos, S.; Schlögl, R.; Savinova, E. R. Operando Evidence for a Universal Oxygen Evolution Mechanism on Thermal and Electrochemical Iridium Oxides. *J. Phys. Chem. Lett.* **2018**, *9*, 3154–3160.
- (26) Pfeifer, V.; Jones, T. E.; Velasco Velez, J. J.; Arrigo, R.; Piccinin, S.; Havecker, M.; Knop-Gericke, A.; Schlögl, R. In situ observation of reactive oxygen species forming on oxygen-evolving iridium surfaces. *Chem. Sci.* **2017**, *8*, 2143–2149.
- (27) Frevel, L. J.; Mom, R.; Velasco-Vélez, J.-J.; Plodinec, M.; Knop-Gericke, A.; Schlögl, R.; Jones, T. E. In Situ X-ray Spectroscopy of the Electrochemical Development of Iridium Nanoparticles in Confined Electrolyte. *J. Phys. Chem. C* **2019**, *123*, 9146–9152.
- (28) Mom, R. V.; Falling, L. J.; Kasian, O.; Algara-Siller, G.; Teschner, D.; Crabtree, R. H.; Knop-Gericke, A.; Mayrhofer, K. J. J.; Velasco-Vélez, J.-J.; Jones, T. E. Operando Structure–Activity–Stability Relationship of Iridium Oxides during the Oxygen Evolution Reaction. *ACS Catal.* **2022**, *12*, 5174–5184.
- (29) Saveleva, V. A.; Wang, L.; Kasian, O.; Batuk, M.; Hadermann, J.; Gallet, J. J.; Bournel, F.; Alonso-Vante, N.; Ozouf, G.; Beauger, C.; Mayrhofer, K. J. J.; Cherevko, S.; Gago, A. S.; Friedrich, K. A.; Zafeirotos, S.; Savinova, E. R. Insight into the Mechanisms of High Activity and Stability of Iridium Supported on Antimony-Doped Tin Oxide Aerogel for Anodes of Proton Exchange Membrane Water Electrolyzers. *ACS Catal.* **2020**, *10*, 2508–2516.
- (30) Velasco-Vélez, J.-J.; Carbonio, E. A.; Chuang, C. H.; Hsu, C. J.; Lee, J. F.; Arrigo, R.; Havecker, M.; Wang, R.; Plodinec, M.; Wang, F. R.; Centeno, A.; Zurutuza, A.; Falling, L. J.; Mom, R. V.; Hofmann, S.; Schlögl, R.; Knop-Gericke, A.; Jones, T. E. Surface Electron-Hole Rich Species Active in the Electrocatalytic Water Oxidation. *J. Am. Chem. Soc.* **2021**, *143*, 12524–12534.
- (31) Lebedev, D.; Ezhov, R.; Heras-Domingo, J.; Comas-Vives, A.; Kaeffer, N.; Willinger, M.; Solans-Monfort, X.; Huang, X.; Pushkar, Y.; Coperet, C. Atomically Dispersed Iridium on Indium Tin Oxide Efficiently Catalyzes Water Oxidation. *ACS Cent. Sci.* **2020**, *6*, 1189–1198.
- (32) Velasco Vélez, J. J.; Bernsmeier, D.; Jones, T. E.; Zeller, P.; Carbonio, E.; Chuang, C. H.; Falling, L. J.; Streibel, V.; Mom, R. V.; Hammud, A.; Havecker, M.; Arrigo, R.; Stotz, E.; Lunkenbein, T.; Knop-Gericke, A.; Krahner, R.; Schlögl, R. The rise of electrochemical NAPXPS operated in the soft X-ray regime exemplified by the oxygen evolution reaction on IrOx electrocatalysts. *Faraday Discuss.* **2022**, *236*, 103–125.
- (33) Urakawa, A.; Bürgi, T.; Baiker, A. Sensitivity enhancement and dynamic behavior analysis by modulation excitation spectroscopy: Principle and application in heterogeneous catalysis. *Chem. Eng. Sci.* **2008**, *63*, 4902–4909.
- (34) Schmidt, T. J.; Gasteiger, H. A.; Stab, G. D.; Urban, P. M.; Kolb, D. M.; Behm, R. J. Characterization of High-Surface-Area Electrocatalysts Using a Rotating Disk Electrode Configuration. *J. Electrochem. Soc.* **1998**, *145*, 2354–2358.
- (35) Diklić, N.; Clark, A. H.; Herranz, J.; Diercks, J. S.; Aegerter, D.; Nachttegaal, M.; Beard, A.; Schmidt, T. J. Potential Pitfalls in the Operando XAS Study of Oxygen Evolution Electrocatalysts. *ACS Energy Lett.* **2022**, *7*, 1735–1740.
- (36) Müller, O.; Nachttegaal, M.; Just, J.; Lutzenkirchen-Hecht, D.; Frahm, R. Quick-EXAFS setup at the SuperXAS beamline for in situ X-ray absorption spectroscopy with 10 ms time resolution. *J. Synchrotron Radiat.* **2016**, *23*, 260–266.
- (37) Clark, A. H.; Steiger, P.; Bornmann, B.; Hitz, S.; Frahm, R.; Ferri, D.; Nachttegaal, M. Fluorescence-detected quick-scanning X-ray absorption spectroscopy. *J. Synchrotron Radiat.* **2020**, *27*, 681–688.
- (38) Saveleva, V. A.; Ebner, K.; Ni, L.; Smolentsev, G.; Klose, D.; Zitolo, A.; Marelli, E.; Li, J.; Medarde, M.; Safonova, O. V.; Nachttegaal, M.; Jaouen, F.; Kramm, U. I.; Schmidt, T. J.; Herranz, J. Potential-Induced Spin Changes in Fe/N/C Electrocatalysts Assessed by In Situ X-ray Emission Spectroscopy. *Angew. Chem., Int. Ed.* **2021**, *60*, 11707–11712.
- (39) Ravel, B.; Newville, M. ATHENA, ARTEMIS, HEPHAESTUS: data analysis for X-ray absorption spectroscopy using IFEFFIT. *J. Synchrotron Radiat.* **2005**, *12*, 537–541.
- (40) Clark, A. H.; Imbao, J.; Frahm, R.; Nachttegaal, M. ProQEXAFS: a highly optimized parallelized rapid processing software for QEXAFS data. *J. Synchrotron Radiat.* **2020**, *27*, 551–557.
- (41) Baurecht, D.; Fringeli, U. P. Quantitative modulated excitation Fourier transform infrared spectroscopy. *Rev. Sci. Instrum.* **2001**, *72*, 3782–3792.
- (42) Oakton, E.; Lebedev, D.; Povia, M.; Abbott, D. F.; Fabbri, E.; Fedorov, A.; Nachttegaal, M.; Copéret, C.; Schmidt, T. J. IrO<sub>2</sub>-TiO<sub>2</sub>: A High-Surface-Area, Active, and Stable Electrocatalyst for the Oxygen Evolution Reaction. *ACS Catal.* **2017**, *7*, 2346–2352.
- (43) Oakton, E.; Lebedev, D.; Fedorov, A.; Krumeich, F.; Tillier, J.; Sereda, O.; Schmidt, T. J.; Copéret, C. A simple one-pot Adams method route to conductive high surface area IrO<sub>2</sub>-TiO<sub>2</sub> materials. *New J. Chem.* **2016**, *40*, 1834–1838.
- (44) Williams, D. B.; Carter, C. B. *Transmission Electron Microscopy A Textbook for Materials Science*; Springer Science + Business Media, 2009; pp 389–405.
- (45) Inorganic Crystal Structure Database. <https://icsd.fiz-karlsruhe.de/search/basic.xhtml> (accessed June 19, 2022).
- (46) Freakley, S. J.; Ruiz-Esquius, J.; Morgan, D. J. The X-ray photoelectron spectra of Ir, IrO<sub>2</sub> and IrCl<sub>3</sub> revisited. *Surf. Interface Anal.* **2017**, *49*, 794–799.
- (47) Lettenmeier, P.; Majchel, J.; Wang, L.; Saveleva, V. A.; Zafeirotos, S.; Savinova, E. R.; Gallet, J. J.; Bournel, F.; Gago, A. S.; Friedrich, K. A. Highly active nano-sized iridium catalysts: synthesis and operando spectroscopy in a proton exchange membrane electrolyzer. *Chem. Sci.* **2018**, *9*, 3570–3579.
- (48) Yu, H.; Danilovic, N.; Wang, Y.; Willis, W.; Poozhikunnath, A.; Bonville, L.; Capuano, C.; Ayers, K.; Maric, R. Nano-size IrOx catalyst of high activity and stability in PEM water electrolyzer with ultra-low iridium loading. *Appl. Catal., B* **2018**, *239*, 133–146.
- (49) Pfeifer, V.; Jones, T. E.; Wrabetz, S.; Massue, C.; Velasco Velez, J. J.; Arrigo, R.; Scherzer, M.; Piccinin, S.; Havecker, M.; Knop-Gericke, A.; Schlögl, R. Reactive oxygen species in iridium-based OER catalysts. *Chem. Sci.* **2016**, *7*, 6791–6795.
- (50) Binninger, T.; Fabbri, E.; Patru, A.; Garganourakis, M.; Han, J.; Abbott, D. F.; Sereda, O.; Kötter, R.; Menzel, A.; Nachttegaal, M.; Schmidt, T. J. Electrochemical Flow-Cell Setup for In Situ X-ray Investigations. *J. Electrochem. Soc.* **2016**, *163*, H906–H912.

- (51) Diercks, J. S.; Herranz, J.; Georgi, M.; Diklić, N.; Chauhan, P.; Ebner, K.; Clark, A. H.; Nachtegaal, M.; Eychmüller, A.; Schmidt, T. J. Interplay between Surface-Adsorbed CO and Bulk Pd Hydride under CO<sub>2</sub>-Electroreduction Conditions. *ACS Catal.* **2022**, *12*, 10727–10741.
- (52) Povia, M.; Herranz, J.; Binniger, T.; Nachtegaal, M.; Diaz, A.; Kohlbrecher, J.; Abbott, D. F.; Kim, B.-J.; Schmidt, T. J. Combining SAXS and XAS To Study the Operando Degradation of Carbon-Supported Pt-Nanoparticle Fuel Cell Catalysts. *ACS Catal.* **2018**, *8*, 7000–7015.
- (53) Mo, Y.; Stefan, I. C.; Cai, W. B.; Dong, J.; Carey, P.; Scherson, D. A. In Situ Iridium LIII-Edge X-ray Absorption and Surface Enhanced Raman Spectroscopy of Electrodeposited Iridium Oxide Films in Aqueous Electrolytes. *J. Phys. Chem. B* **2002**, *106*, 3681–3686.
- (54) Minguzzi, A.; Lugaesi, O.; Achilli, E.; Locatelli, C.; Vertova, A.; Ghigna, P.; Rondinini, S. Observing the oxidation state turnover in heterogeneous iridium-based water oxidation catalysts. *Chem. Sci.* **2014**, *5*, 3591–3597.
- (55) Nong, H. N.; Falling, L. J.; Bergmann, A.; Klingenhof, M.; Tran, H. P.; Spori, C.; Mom, R.; Timoshenko, J.; Zichittella, G.; Knop-Gericke, A.; Piccinin, S.; Perez-Ramirez, J.; Cuenya, B. R.; Schlögl, R.; Strasser, P.; Teschner, D.; Jones, T. E. Key role of chemistry versus bias in electrocatalytic oxygen evolution. *Nature* **2020**, *587*, 408–413.
- (56) Roth, C.; Benker, N.; Buhrmester, T.; Mazurek, M.; Loster, M.; Fuess, H.; Koningsberger, D. C.; Ramaker, D. E. Determination of O[H] and CO Coverage and Adsorption Sites on PtRu Electrodes in an Operating PEM Fuel Cell. *J. Am. Chem. Soc.* **2005**, *127*, 14607–14615.
- (57) Teliska, M.; O'Grady, W. E.; Ramaker, D. E. Determination of O and OH Adsorption Sites and Coverage in Situ on Pt Electrodes from Pt L23 X-ray Absorption Spectroscopy. *J. Phys. Chem. B* **2005**, *109*, 8076–8084.
- (58) Arruda, T. M.; Shyam, B.; Ziegelbauer, J. M.; Mukerjee, S.; Ramaker, D. E. Investigation into the Competitive and Site-Specific Nature of Anion Adsorption on Pt Using In Situ X-ray Absorption Spectroscopy. *J. Phys. Chem. C* **2008**, *112*, 18087–18097.
- (59) Kongkanand, A.; Ziegelbauer, J. M. Surface Platinum Electrooxidation in the Presence of Oxygen. *J. Phys. Chem. C* **2012**, *116*, 3684–3693.
- (60) Ishiguro, N.; Saida, T.; Uruga, T.; Nagamatsu, S.-i.; Sekizawa, O.; Nitta, K.; Yamamoto, T.; Ohkoshi, S.-i.; Iwasawa, Y.; Yokoyama, T.; Tada, M. Operando Time-Resolved X-ray Absorption Fine Structure Study for Surface Events on a Pt<sub>3</sub>Co/C Cathode Catalyst in a Polymer Electrolyte Fuel Cell during Voltage-Operating Processes. *ACS Catal.* **2012**, *2*, 1319–1330.
- (61) Ishiguro, N.; Kityakarn, S.; Sekizawa, O.; Uruga, T.; Sasabe, T.; Nagasawa, K.; Yokoyama, T.; Tada, M. Rate Enhancements in Structural Transformations of Pt–Co and Pt–Ni Bimetallic Cathode Catalysts in Polymer Electrolyte Fuel Cells Studied by in Situ Time-Resolved X-ray Absorption Fine Structure. *J. Phys. Chem. C* **2014**, *118*, 15874–15883.
- (62) Ebner, K.; Clark, A. H.; Saveleva, V. A.; Smolentsev, G.; Chen, J.; Ni, L.; Li, J.; Zitolo, A.; Jaouen, F.; Kramm, U. I.; Schmidt, T. J.; Herranz, J. Time-Resolved Potential-Induced Changes in Fe/N/C-Catalysts Studied by In Situ Modulation Excitation X-Ray Absorption Spectroscopy. *Adv. Energy Mater.* **2022**, *12*, No. 2103699.
- (63) Mayrhofer, K. J. J.; Bliznac, B. B.; Arenz, M.; Stamenkovic, V. R.; Ross, P. N.; Markovic, N. M. The Impact of Geometric and Surface Electronic Properties of Pt-Catalysts on the Particle Size Effect in Electrocatalysis. *J. Phys. Chem. B* **2005**, *109*, 14433–14440.
- (64) Osmieri, L.; Ahluwalia, R. K.; Wang, X.; Chung, H. T.; Yin, X.; Kropf, A. J.; Park, J.; Cullen, D. A.; More, K. L.; Zelenay, P.; Myers, D. J.; Neyerlin, K. C. Elucidation of Fe-N-C electrocatalyst active site functionality via in-situ X-ray absorption and operando determination of oxygen reduction reaction kinetics in a PEFC. *Appl. Catal., B* **2019**, *257*, No. 117929.
- (65) Kavakli, C.; Meini, S.; Harzer, G.; Tsiouvaras, N.; Piana, M.; Siebel, A.; Garsuch, A.; Gasteiger, H. A.; Herranz, J. Nanosized Carbon-Supported Manganese Oxide Phases as Lithium-Oxygen Battery Cathode Catalysts. *ChemCatChem* **2013**, *5*, 3358–3373.
- (66) Pedersen, A. F.; Escudero-Escribano, M.; Sebok, B.; Bodin, A.; Paoli, E.; Frydendal, R.; Friebe, D.; Stephens, I. E. L.; Rossmeisl, J.; Chorkendorff, I.; Nilsson, A. Operando XAS Study of the Surface Oxidation State on a Monolayer IrO<sub>x</sub> on RuO<sub>x</sub> and Ru Oxide Based Nanoparticles for Oxygen Evolution in Acidic Media. *J. Phys. Chem. B* **2018**, *122*, 878–887.
- (67) Ferri, D.; Newton, M. A.; Nachtegaal, M. Modulation Excitation X-Ray Absorption Spectroscopy to Probe Surface Species on Heterogeneous Catalysts. *Top. Catal.* **2011**, *54*, 1070–1078.
- (68) Laguna-Marco, M. A.; Arias-Egido, E.; Piquer, C.; Cuartero, V.; Hernández-López, L.; Kayser, P.; Alonso, J. A.; Barker, J. A. T.; Fabbri, G.; Escanhoela, C. A.; Irifune, T. Magnetism of Ir<sup>5+</sup>-based double perovskites: Unraveling its nature and the influence of structure. *Phys. Rev. B* **2020**, *101*, No. 014449.
- (69) Cao, G.; Qi, T. F.; Li, L.; Terzic, J.; Yuan, S. J.; DeLong, L. E.; Murthy, G.; Kaul, R. K. Novel magnetism of Ir<sup>5+</sup>(5d<sup>4</sup>) Ions in the double perovskite Sr<sub>2</sub>YIrO<sub>6</sub>. *Phys. Rev. Letters* **2014**, *112*, No. 056402.
- (70) Laguna-Marco, M. A.; Kayser, P.; Alonso, J. A.; Martínez-Lope, M. J.; van Veenendaal, M.; Choi, Y.; Haskel, D. Electronic structure, local magnetism, and spin-orbit effects of Ir(IV)-, Ir(V)-, and Ir(VI)-based compounds. *Phys. Rev. B* **2015**, *91*, No. 214433.
- (71) Kayser, P.; Martínez-Lope, M. J.; Alonso, J. A.; Retuerto, M.; Croft, M.; Ignatov, A.; Fernández-Díaz, M. T. Crystal and Magnetic Structure of Sr<sub>2</sub>MIrO<sub>6</sub> (M = Ca, Mg) Double Perovskites—A Neutron Diffraction Study. *Eur. J. Inorg. Chem.* **2014**, *2014*, 178–185.

## Recommended by ACS

### Deteriorated Balance between Activity and Stability via Ru Incorporation into Ir-Based Oxygen Evolution Nanostructures

Kyu-Su Kim, Yong-Tae Kim, *et al.*

AUGUST 11, 2023

ACS CATALYSIS

READ 

### Degradation Mechanism of Calcium Iridium Oxide for Oxygen Evolution Reaction in Acid

Ruihan Li, Linsey Seitz, *et al.*

AUGUST 15, 2023

ENERGY & FUELS

READ 

### Revisiting the Activity Gap of Iridium Electrocatalysts for Acidic Water Oxidation

Jiajian Gao, Kuo-Wei Huang, *et al.*

JULY 13, 2023

THE JOURNAL OF PHYSICAL CHEMISTRY LETTERS

READ 

### Lithium-Directed Transformation of Amorphous Iridium (Oxy)hydroxides To Produce Active Water Oxidation Catalysts

Jonathan Ruiz Esquivias, Simon J. Freakley, *et al.*

MARCH 09, 2023

JOURNAL OF THE AMERICAN CHEMICAL SOCIETY

READ 

Get More Suggestions >